Materials and Structures (2017) 50:237
https://doi.org/10.1617/s11527-017-1094-7

ORIGINAL ARTICLE

Capacitance-based defect detection and defect location determination for cement-based material

Yulin Wang · D. D. L. Chung

Received: 6 June 2017 / Accepted: 8 September 2017 / Published online: 24 October 2017

Abstract This paper provides the first report of capacitance-based nondestructive cement-based material defect detection. It is based on the use of the fringing electric field (2 kHz) of a capacitor that comprises the cement-based material (cement paste slab, 250 × 250 × 9.31 mm^3) and two relatively small copper electrodes separated from the slab by an electrically insulating polymer film. Due to the fringing field through the slab, the apparent permittivity is high, thus enabling the measured capacitance to be sensitive to defects. The through-thickness capacitance, which relates to the apparent relative permittivity of the cement-based material, is measured using electrodes that sandwich the slab. The in-plane capacitance is measured using closely spaced parallel coplanar electrodes. A region (150 × 150 × 9.31 mm^3) of the slab is rendered defective by containing gypsum pellets, the porosity of which causes the apparent relative permittivity of this region (142) to be lower than that of the adjacent perfect region (199). To determine the position of the boundary of the defective region, the capacitance is measured using a series of electrodes, with each electrode geometry consisting of *N* squares linearly aligned perpendicular to the boundary. The capacitance is measured in order of increasing *N*, which is sufficient for the electrode to cover regions on both sides of the boundary. The capacitance increases linearly with *N* in each region, with the slope being different for the two regions. The intersection of the extrapolated linear curves of the two regions gives the position of the boundary.

Keywords Cement · Concrete · Capacitance · Permittivity · Defect · Nondestructive evaluation · Fringing electric field

1 Introduction

Due to the aging of the civil infrastructure, nondestructive evaluation (NDE) of cement-based materials is critically needed for enhancing public safety. The NDE methods include microwave, electromagnetic and impedance methods [1–6], electrical resistivity methods [7], electrochemical methods [8–10], ultrasonic and acoustic methods [11–20], stress wave methods [21], X-ray methods [22–28], gamma ray methods [29], infrared spectroscopy [30], vibrational

Y. Wang · D. D. L. Chung (✉)
Composite Materials Research Laboratory, Department of Mechanical and Aerospace Engineering, University at Buffalo, The State University of New York, Buffalo, NY 14260-4400, USA
e-mail: ddlchung@buffalo.edu
URL: http://alum.mit.edu/www/ddlchung

Present Address:
Y. Wang
College of Civil Engineering and Architecture, Wuyi University, Wuyi Road 16, Xinfeng Street, Wuyi Shan City 354300, Fujian Province, China

and stress methods [31–40], air permeability testing [41], and nuclear magnetic resonance (NMR) [42, 43].

Electrical resistivity measurements are effective for detecting defects only if the defects cause substantial change in the resistivity of the material. In addition, resistivity measurements have strict requirements on the quality of the electrical contacts and the quality may not be cost-effectively realized in the field. The reflection of ultrasonic or radio wave off the surface of a defect (such as a crack) with a well-defined and substantial surface is effective for detecting the defect, but defects that do not adequately present such surfaces cannot be effectively detected. Vibrational and stress methods are based on the effect of defects on the mechanical properties (such as the elastic modulus) of the material; their use requires mechanical loading, which may not be desirable for the structure. Electrochemical methods are based on the effect of defects on the electrochemical properties, such as the potential and current associated with corrosion; their use requires an electrolyte, an anode and a cathode for enabling the electrochemical reaction. Air permeability testing is based on the effect of defects on the air permeability; its effectiveness requires that the defects are capable of affecting the air permeability substantially. Infrared spectroscopy and NMR are chemical analysis techniques that are commonly used in the laboratory, but their effectiveness for defect detection in a solid is limited, unless the defect has a substantial effect on the infrared absorption or NMR characteristics. X-ray and gamma ray methods are effective for detecting defects, provided that the defects are sufficiently different from the perfect part of the material in the ability to absorb the radiation.

Instrumentation portability is valuable for NDE in the field. X-ray, gamma ray, infrared spectroscopy, NMR and microwave methods tend to involve instrumentation that is not portable. In contrast, electrical, ultrasonic and electrochemical methods involve portable instrumentation. Electrical methods are particularly attractive, due to the instrumentation portability, fast response and suitability for real-time monitoring.

The electrical or electromagnetic behavior is described by the impedance, which relates to the resistance (related to the electrical conductivity) and the capacitance (related to the electric permittivity). The resistance is increased by the presence of flaws [44, 45]. However, the measurement of the resistance is complicated by the tendency for the cement-based material to polarize, though the polarization can be reduced by the addition of electrically conductive admixtures such as short carbon fibers [46–48]. The polarization causes the measured resistance to be higher than the true resistance.

The permittivity of cement-based materials does not vary over a wide range upon loading [49] or upon admixture addition [50], so the permittivity is not sufficiently sensitive to the flaws or microstructure, as needed for NDE. However, we recently reported that, when the capacitance is unconventionally measured using electrical contacts (electrodes) that are smaller in area than the cement-based material being sandwiched by the electrical contacts, the fringing electric field is large and greatly increases the apparent (measured) relative permittivity of the cement-based material [51]. The apparent relative permittivity (2 kHz) increases with increasing thickness, due to the increasing fringing field with increasing thickness. For plain cement paste of various thicknesses, it ranges from 150 to 375. In contrast, when the electrical contacts conventionally cover the entire area of the cement-based material, the fringing field effect is much weaker, so that the apparent relative permittivity is much lower, ranging from 24 to 38 for plain cement paste of various thicknesses. Therefore, in this paper, we investigate for the first time the use of the high capacitance associated with the high apparent relative permittivity to probe the defective region of a cement-based slab.

The objectives of this work are (1) to demonstrate the feasibility of using capacitance measurement to probe the defective region of a cement-based slab for defect detection and defect location determination, (2) to investigate the effects of defects on the dielectric behavior of a cement-based material, and (3) to provide a new NDE method for cement-based materials. The materials investigated are cement pastes without and with artificially incorporated flaws.

2 Methods

2.1 Materials

Portland cement (Type I, ASTM C150, from Lafarge Corp., Southfield, MI) is used. The water/cement ratio is 0.35. No aggregate is used.

Silica fume (Elkem Materials Inc., Pittsburgh, PA, microsilica, EMS 965, USA) is used at 15% by mass of cement, as in prior work [52]; it has particle size ranging from 0.03 to 0.5 μm, with average size 0.2 μm; it contains >93 wt.% SiO_2, <0.7 wt.% Al_2O_3, <0.7 wt.% CaO, <0.7 wt.% MgO, <0.5 wt.% Fe_2O_3, <0.4 wt.% Na_2O, <0.9 wt.% K_2O, and <6 wt.% loss on ignition. The silica fume has been subjected to silane treatment in order to improve its dispersion in the cement mix [53, 54]. The silane coupling agent is a 1:1 (by mass) mixture of Z-6020 ($H_2NCH_2CH_2NHCH_2CH_2CH_2Si(OCH_3)_3$) and Z-6040 ($OCH_2$-$CHCH_2OCH_2CH_2CH_2Si(OCH_3)_3$) from Dow Corning Corp. (Midland, MI). The amine group in Z-6020 serves as a catalyst for the curing of the epoxy and consequently allows the Z-6020 molecule to attach to the epoxy end of the Z-6040 molecule. The trimethylsiloxy ends of the Z-6020 and Z-6040 molecules then connect to the –OH functional group on the surface of the silica fume. The silane is dissolved in ethylacetate to form a solution with 2.0 wt.% silane. Surface treatment of the silica fume is performed by immersion in the silane solution, heating to 75 °C while stirring, and then holding at 75 °C for 1.0 h, followed by filtration and drying. Subsequently, the silica fume is heated at 110 °C for 12 h [53, 54].

A high-range water reducing agent (Glenium 3000NS, BASF Construction Chemicals) is used at 1.0% by mass of cement. The defoamer (Colloids Inc., Marietta, GA, 1010, USA) is used at 0.13% (% of specimen volume).

All the ingredients are mixed in a rotary mixer with a flat beater. Square oiled plastic molds of dimensions 250 × 250 × 9.31 mm are used to produce specimens of the same size. For all specimens, after filling the mold, an external vibrator is used to facilitate compaction and diminish the air bubbles. The specimens are demolded after 24 h and then cured at a relative humidity of nearly 100% for 28 days.

A defective region of size 150 × 150 mm is formed at a corner of the 250 × 250 mm slab (Fig. 1) by pouring cement paste that contains gypsum pellets (Fig. 2) into this region of the mold, as defined prior to and during the pouring by using cardboard separators of thickness 0.68 mm. Plain cement paste (without gypsum) is poured into the remaining region of the mold. The separator is removed at 15 min after pouring.

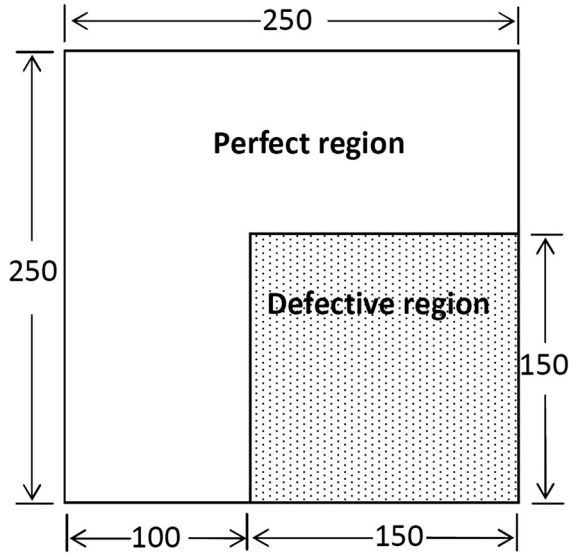

Fig. 1 Cement-based slab with a perfect region (plain cement paste) and a defective region (cement paste with gypsum pellets). All dimensions are in mm. The perfect region does not contain gypsum. The defective region contains gypsum

Fig. 2 Gypsum particles used as an admixture to provide defective cement paste. The scale nearest the gypsum particles has the smallest division in mm

The gypsum pellets of density 0.8385 g/cm^3 and average size 4.3 mm are prepared by smashing a gypsum block that includes in its mix design cement in the amount of 5% by mass of the gypsum. The gypsum block is made from gypsum powder (Type Quick Set provided by National Gypsum).

Cement powder and silica fume are dry mixed by using a rotary mixer with a flat beater without water addition for about 3 min. Then, the mixture is divided into two portions. One portion amounts to 64% of the total weight of the mix and the other portion amounts to 36% of the total weight. The 36% portion is then

mixed with the gypsum pellets in the amount of 20% by mass of cement by using the rotary mixer for 2 min, and then water (0.35 by mass of cement) is gradually added to the mixture while mixing continues for an additional period of 5 min. After this, the mixture containing gypsum pellets is poured into the 150 × 150 mm corner part of the mold. Finally, the 64% portion is mixed by using the rotary mixer for 2 min, and water (0.35 by mass of cement) is gradually added to the mixture while mixing is continued for an additional period of 5 min, followed by pouring into the remaining part of the mold.

The specimens (slabs) are demolded after 24 h, and then cured at a relative humidity of nearly 100% for 28 days. The demolded specimens are ground and burnished to ensure that the surfaces are smooth before capacitance measurement.

2.2 Methodology

2.2.1 Permittivity measurement

The measurement of the relative permittivity typically involves a parallel-plate capacitor configuration, with the specimen under investigation being sandwiched by electrodes [50]. There is an electrically insulating (dielectric) plastic film positioned between the specimen and each electrode, as necessitated by the fact that the RLC meter used for the capacitance measurement is not designed for measuring the capacitance of a conductive material. In this work, this film is simply a commercial double-sided adhesive tape. Although cement in the absence of a conductive admixture is only slightly conductive, the use of an insulating film is recommended and used in this work. The electrodes are in the form of copper foils. The electrode, plastic sheet and cement-based specimen are held together by adhesion.

The relative permittivity κ in the direction perpendicular to the plane of the sandwich is given by the equation

$$C_v = \varepsilon_o \kappa A_s / l, \tag{1}$$

where C_v is the capacitance due to the volume of the specimen, ε_o is the permittivity of free space (8.85×10^{-12} F/m), A_s is the area of the sandwich (i.e., the area of the electrode), and l is the thickness of the specimen sandwiched by the electrodes.

The fringing electric field refers to the electric field in the surrounding medium immediately beyond the rim of the specimen in the parallel-plate capacitor geometry. The fringing field results in the measured capacitance to be higher than the expected value. This is because the fringing electric field causes the specimen area to be effectively larger than the true area. As a consequence, the measured (apparent) permittivity is higher than the true value. The higher is the permittivity of the surrounding medium, the greater is the fringing field effect and the higher is the apparent permittivity. In this work, the surrounding medium is the cement-based material being evaluated, as provided by the use of electrodes that are smaller in area than the cement-based material [51].

2.2.2 Decoupling the volumetric and interfacial contributions to the measured capacitance

The interface between the specimen and the electrode (whether there is an insulating film at the interface or not) affects the measured capacitance. A method of decoupling the volumetric and interfacial contributions to the measured capacitance involves testing multiple sandwiches with different areas, but the same thickness [51]. This is illustrated in Fig. 3 for three areas that are equal to the areas of 1, 2 and 3 squares that are in contact and lined up along an edge of the square in the same plane and the same direction. The measured capacitance C_m is given by the equation for capacitances in parallel, i.e.,

$$C_m = C_o + \varepsilon_o \kappa NA / l, \tag{2}$$

where N is the number of squares that constitute the electrode and C_o is the capacitance at $N = 0$. The C_o relates to the fringing field effect, as obtained by

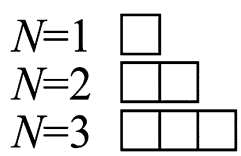

Fig. 3 Electrode configuration in the form of rectangles consisting of 1, 2 or 3 squares that are lined up. The integer N refers to the number of square lined up. The area of each square slab is A

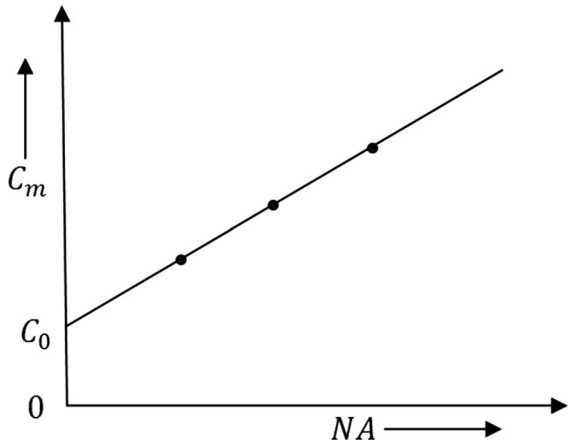

Fig. 4 Schematic plot of C_m versus the area NA, where N is the number of squares that make up an electrode (Fig. 3) and A is the area of each square

extrapolating the plot of C_m versus NA to $N = 0$ (Fig. 4). This method of permittivity measurement is as previously reported and shown to be reliable [51]. Based on Eq. (2), the slope of the plot of C_m versus NA is equal to $\varepsilon_o \kappa/l$. Thus, κ is obtained from the slope. Since the interface is structural identical for all values of NA, the slope effectively removes the interfacial contribution. In case that the electrodes are smaller than the cement-based specimen, the fringing field effect is large and the κ obtained from the slope is the apparent relative permittivity.

2.2.3 *Spatially resolved capacitance measurement*

By positioning the electrodes at different points of the cement-based specimen, spatially resolved capacitance measurement is achieved. The capacitance is measured in either the through-thickness direction (configuration A, Fig. 5) or the in-plane direction (configuration B, Fig. 6). The electrodes are either square (for $N = 1$) or rectangular (for $N > 1$), with width equal to 25.0 mm and length equal to the combined length of N squares (Fig. 4). The left edge of the electrode is at a distance of 10.0 mm from the left edge of the slab.

In configuration A, the electrodes are directly on top of one another and sandwich the specimen, which extend beyond the electrodes. Configuration A allows determination of the apparent permittivity, because the cross-sectional area of the current path is well defined (except for the fringing field increasing this

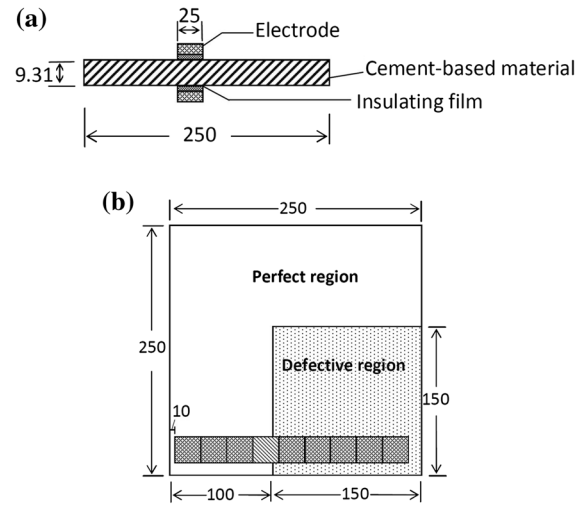

Fig. 5 Configuration A for defect detection, using two electrodes (area = 25N mm × 25 mm, where $N = 1, 2,\ldots, 9$) at the same location on the opposite surfaces of the slab (250 × 250 × 9.31 mm). An electrically insulating film is positioned between the cement-based specimen and the entire area of each electrode. All dimensions are in mm. **a** Side view, showing the 25-mm edge of one of the locations of the electrode. **b** Top view, showing a series of electrodes for $N = 1, 2,\ldots, 9$, with one of the 25 × 25 mm squares (the fourth square from the left) striding across the boundary between the perfect region (plain cement paste) and the defective region (cement paste with gypsum particles), and with the left edge of the electrode at a distance of 10.0 mm from the left edge of the slab. The series of electrodes shown is perpendicular to the left boundary of the defective region, thus allowing determination of the location of this boundary. By using a series of electrodes (not shown) that is perpendicular to the top boundary of the defective region, the position of this boundary is determined. The perfect region does not contain gypsum. The defective region contains gypsum

area beyond the electrode area). In configuration B, the electrodes are coplanar on the same surface of the specimen, such that they are parallel to one another, with their proximate edges at a distance g apart, with $g = 15$, 30, 60 and 90 mm. Configuration B does not allow determination of the apparent permittivity, because the current spreads between the two coplanar electrodes. The spreading causes the cross-sectional area of the current path to be inadequately defined. Nevertheless, configuration B is more convenient than configuration A for application to structures, which may not be conveniently accessed from both top and bottom surfaces.

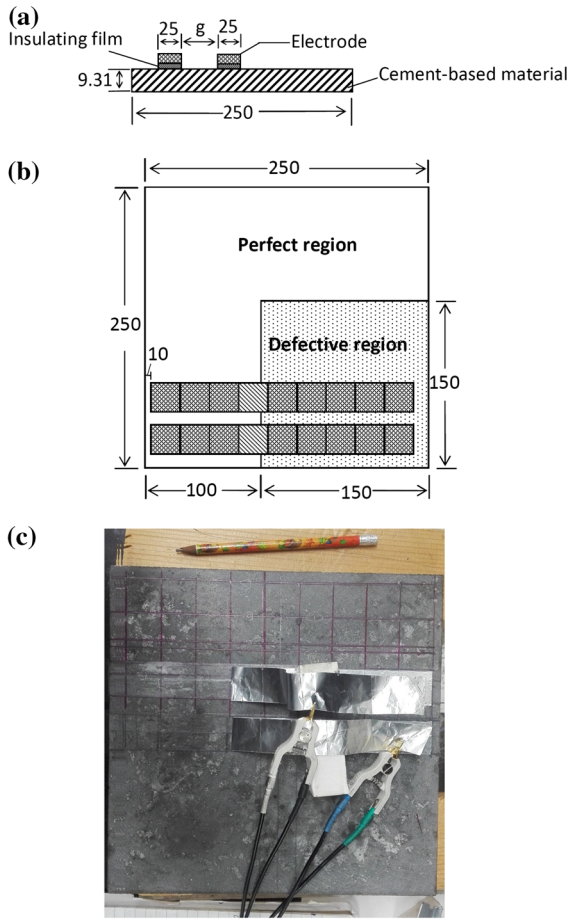

◀**Fig. 6** Configuration B for defect detection, using two coplanar electrodes (area = 25 N × 25 mm, where N = 1, 2,…, 9) on the same surface of the slab (250 × 250 × 9.31 mm), with the proximate edges of the two electrodes separated by a distance g. An electrically insulating film is positioned between the cement-based specimen and the entire area of each electrode. All dimensions are in mm. **a** Side view, showing the 25-mm edge of each of the two electrodes. **b** Top view, showing a series of nine pairs of electrode for N = 1, 2,…, 9, with one of the 25 × 25 mm squares (the fourth square from the left) striding across the boundary between the perfect region (plain cement paste) and the defective region (cement paste with gypsum particles), and with the left edge of the electrode at a distance of 10.0 mm from the left edge of the slab. The two electrodes in each pair have the same value of N and their proximate edges are separated by a distance g. The series of electrode pairs shown is perpendicular to the left boundary of the defective region, thus allowing determination of the location of this boundary. By using a series of electrode pairs (not shown) that is perpendicular to the top boundary of the defective region, the position of this boundary is determined. The perfect region does not contain gypsum. The defective region contains gypsum. **c** Photo of the testing configuration, showing two strips of aluminum foil attached to the specimen, with each strip having a portion that is not attached to facilitate electrical connection to the strip by the use of a clip. This photo also shows 25 mm × 25 mm squares manually drawn on the specimen surface to guide the aluminum foil attachment

2.2.4 *Determination of the boundary between the perfect and defective regions*

In both configurations A and B (Figs. 5, 6), N ranges from 1 to 9 and capacitance measurement is progressively conducted in order of increasing N. One of the nine 25 × 25 mm squares (the fourth square from the left) strides across the boundary between the perfect region (plain cement paste, without gypsum particles) and the defective region (cement paste with gypsum pellets).

Figure 7 applies to both configurations and shows the schematic plot of C_m versus NA. The slope of this plot differs between the perfect region and the defective region, due to the lower apparent permittivity of the defective region. The intersection of the extrapolated linear curves of the two sides gives the position of the boundary between the two regions. Because the fourth square from the left edge of the slab strides across this boundary, as shown in Figs. 5b and 6b, the data point corresponding to $N = 4$ is not included in the data points used for obtaining the linear curve for the perfect region. Hence, N = 1, 2 and 3 are used for obtaining the linear curve for the perfect region, whereas N = 5, 6, 7, 8 and 9 are used for obtaining the linear curve for the defective region.

By using a series of electrodes that are oriented perpendicular to the left boundary of the defective region, the location of this boundary is determined. By using a series of electrodes that are oriented perpendicular to the top boundary of the defective region, the location of this boundary is determined.

2.2.5 *Instrumentation*

The capacitance is measured using a precision RLC meter (QuadTech Model 7600). For configuration A, the through-thickness electric field is 0.027 V/cm. For configuration B, the in-plane electric field corresponds to that of a fixed voltage of 0.25 V between the two coplanar electrodes across the distance g, which is varied. The frequency is 2 kHz. The measured capacitance is that for the equivalent circuit model in which the capacitance and resistance in parallel.

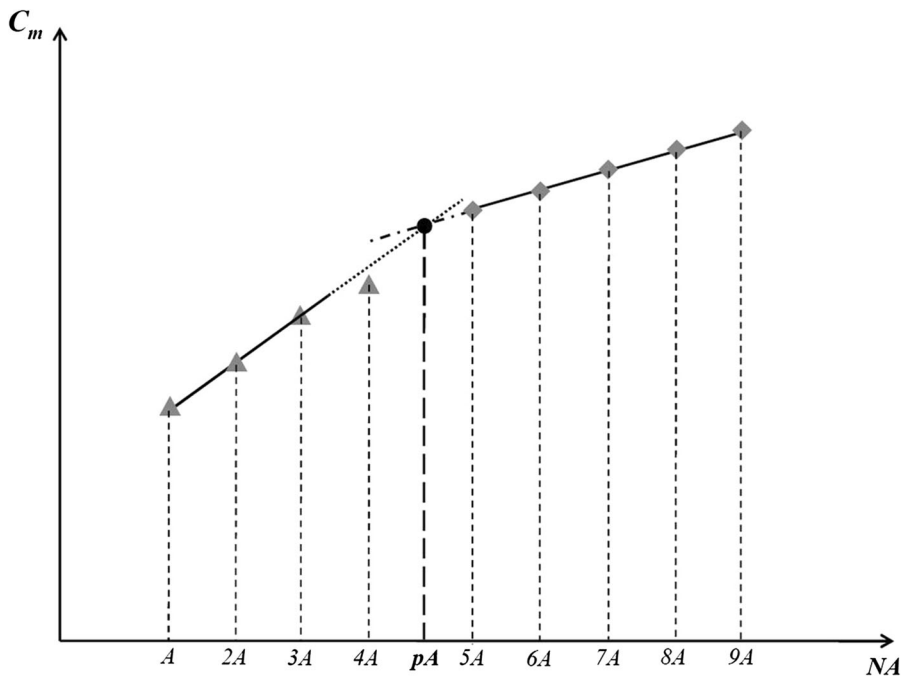

Fig. 7 Schematic plot of capacitance C versus electrode area NA (with $N = 1, 2, \ldots, 9$), illustrating the method of determining the interface located at pA (where p, which is not necessarily integral, is the number of squares in the electrode geometry in the perfect region) between the perfect region (left of pA) and the defective region (right of pA). This illustration applies to both configurations A and B. This interface is given by the intersection of two extrapolated linear curves (shown by dashed lines) on the two sides of the interface. The slope of the linear curve is smaller for the defective region than the perfect region, due to the lower apparent permittivity of the defective region

2.2.6 Difference from impedance spectroscopy

This work uses a technique that differs greatly from the widely used technique of impedance spectroscopy, which measures the impedance as a function of frequency and uses the frequency dependence to obtain information. Firstly, the technique of this work does not measure the impedance, but measures the relative permittivity (real part of the permittivity). Secondly, the technique of this work decouples the contribution of the specimen-contact interface from the contribution of the volume of the specimen. This decoupling is not performed in impedance spectroscopy. Thirdly, the technique of this work does not need to address the frequency dependence in order to obtain meaningful information. In contrast, impedance spectroscopy is focused on the frequency dependence of the impedance, as conventionally described in terms of the Nyquist plot, for the purpose of deriving by mathematical fitting of the plot an equivalent electrical circuit that is intended to describe the electrical/dielectric behavior of the material. The circuit model obtained by the curve fitting tends to be not unique, so the determined values of the circuit elements in the model are not very meaningful.

Table 1 Apparent relative permittivity obtained using configuration A

	Perfect region	Defective region
Apparent relative permittivity	198.7 ± 5.7	141.5 ± 6.4

The slab has thickness 9.31 mm. The perfect region does not contain gypsum. The defective region contains gypsum

Table 2 Slope of the curve of the measured capacitance C_m versus electrode area, obtained using configuration B

g (mm)	Perfect region				Defective region			
	15	30	60	90	15	30	60	90
Slope (pF/mm^2)	0.157 ± 0.008	0.142 ± 0.007	0.136 ± 0.004	0.102 ± 0.005	0.105 ± 0.003	0.092 ± 0.007	0.086 ± 0.004	0.070 ± 0.006

The apparent permittivity cannot be obtained using configuration B, because the cross-sectional area of the current path is not well defined. g = distance between the proximate edges of the two electrodes. The perfect region does not contain gypsum. The defective region contains gypsum

3 Experimental confirmation of methodology

Figure 8 shows that the results for both configurations A and B are as illustrated in Fig. 7. For both configurations, the curve on each side of the boundary

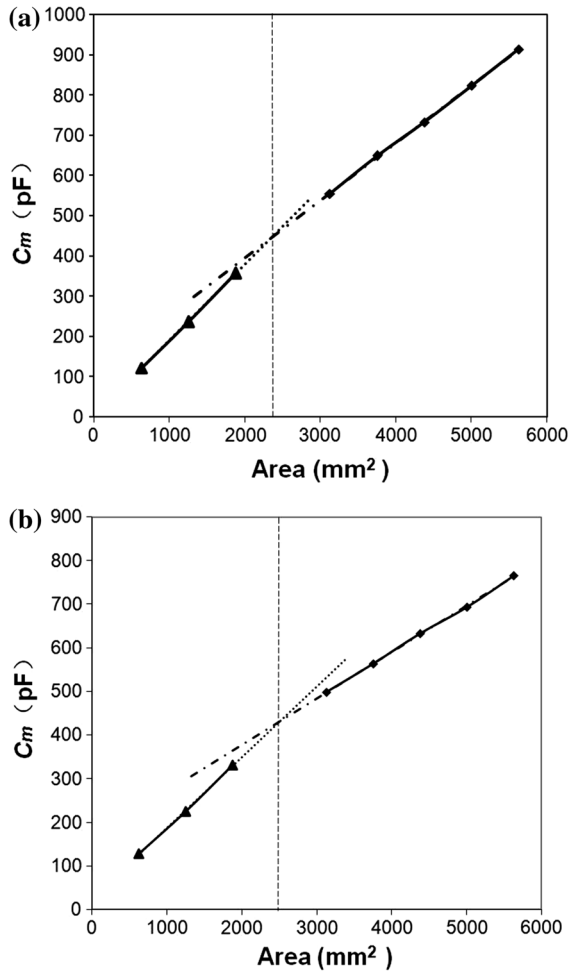

Fig. 8 Dependence of the measured capacitance C_m versus electrode area (pA, where $N = 1, 2, 3, 5, 6, 7, 8$ and 9). The interface between the perfect region (plain cement paste) and the defective region (cement paste with gypsum particles) is indicated by the intersection of two extrapolated linear curves (shown by dashed lines) on the two sides of the interface. **a** Configuration A. The interface is at $pA = 2304.5$ mm^2 and the distance of this interface from the left edge of the electrode is given by $x_0 = pA/(25\text{ mm}) = 92.2$ mm, i.e., the distance of this interface from the left edge of the slab is 102.2 mm, and $p = 3.69$. **b** Configuration B. The interface is thus at $pA = 2469$ mm^2 and the distance of this interface from the left edge of the electrode is given by $pA/(25\text{ mm}) = 98.8$ mm, i.e., the distance of this interface from the left edge of the slab is 108.8 mm, and $p = 3.95$

between the perfect and defective regions is linear, as illustrated in Fig. 7.

Table 1 shows that the apparent relative permittivity obtained using configuration A is lower for the defective region than the perfect region. This is due to the porosity associated with the gypsum in the defective region and the fact that the relative permittivity of air is low (namely 1.0005 [55]).

The value of the apparent relative permittivity of the perfect region (200, Table 1) is similar to the value of 144 previously reported by the same authors [51] for silica fume cement paste using a similar method. The difference in the permittivity is attributed to the differences in specimen dimensions and electrode dimensions.

Table 2 shows that the slope of the curve of the measured capacitance C_m versus electrode area, obtained using configuration B, decreases with increasing g. This is expected, since g relates to the thickness of the capacitor. Thus, for enhancing the sensitivity of the NDE, a low value of g is recommended. For the same value of g, the slope is lower for the defective region than the perfect region, also due to the porosity associated with the gypsum in the defective region.

Figure 9 shows the positions of the boundary of the defective region, as determined by the method of Fig. 7, for configurations A and B. This boundary is located from the transverse edge of the electrode (the electrode edge perpendicular to the length of the electrode and containing the square for $N = 1$, Fig. 7) at distance $pA/25$ *mm*, where A is the area of each square in the electrode geometry and p is the number (not necessarily integral) of squares in the electrode geometry in the perfect region. For configurations A and B, p is 3.69 and 3.95 respectively (Fig. 8). There is some deviation of the determined boundary location from the actual boundary location. Table 3 shows that the error of the distance of the determined boundary location from an edge of the slab is comparable for configurations A and B; the error is mostly below 10%.

The series of squares that constitute an electrode does not need to include a square that strides across the boundary of the defective region, although the striding option is used in this work. This is because the linear curve on each side of the boundary can be established with three or more data points away from the boundary and the intersection of the linear curves of the two sides provides indication of the position of the boundary (Fig. 9).

The boundary of the defective region is straight in this work. However, the boundary of the defective region does not need to be straight, as the measurement is conducted along a line that intersects a particular point along this interface.

By decreasing the size of each square in the electrode series, the error would be reduced. By increasing the size of the slab, the error would also be

Table 3 Determined locations of the interface between the perfect region and the defective region and the error of this determination

Configuration	Location	Left boundary of the defective region		Top boundary of the defective region	
		Determined distance of the boundary from the left edge of the slab (mm)	Error of determined boundary location (%)	Determined distance of the boundary from the top edge of the slab (mm)	Error of determined boundary location (%)
A	1	94.5	5.5	94.1	5.9
	2	102.2	2.2	94.2	5.8
	3	110.5	10.5	98.2	1.8
	4	101.9	1.9	96.9	3.1
B	1	108.8	8.8	93.3	6.7
	2	106.2	6.2	94.7	5.3
	3	106.6	6.6	91.5	8.5
	4	97.2	3.8	93.4	6.6

The locations along the left boundary of the defective region are labeled 1, 2, 3 and 4, in order according to the distance from the bottom edge of the slab. The locations along the top boundary of the defective region are labeled 1, 2, 3 and 4, in order according to the distance from the left boundary of the defective region. The perfect region does not contain gypsum. The defective region contains gypsum

reduced. Since the size of a structural slab is much larger than the size of 250 mm used in this work, the error in practical implementation will be small even using the same square size (25 mm) as this work.

In practical implementation, configuration B is more convenient than configuration A. This is because configuration A requires the presence of electrodes on two opposite surfaces, whereas configuration B requires electrodes on the same surface. The convenience associated with configuration B is particularly great in case that the cement-based structure is large or has non-parallel surfaces. On the other hand, configuration A is advantageous for detecting the internal flaws, particularly when the thickness is large, since the electric field goes through the entire thickness of the material. In contrast, configuration B only detects flaws that are in the surface region, with this limitation being particularly significant when the thickness is large. In general, configurations A and B may be used in a complementary manner for various parts of the same structure.

The implementation of the capacitance method in structures is simple, as it just involves the adhesion of metal foil (e.g., copper foil, aluminum foil, steel foil, etc.) on the cement-based structure. The adhesive agent also serves as an electrically insulating (dielectric layer). Although double-sided adhesive tape is used in this work for the adhesive agent, a variety of polymeric adhesive agents can be used instead. This means that paint, which is also insulating, may not need to be removed prior to the application of the electrodes, in case that the cement-based structure is one that has been painted.

Capacitance measurement and electrical resistance measurement are the two main types of electrical measurement. The capacitance method is simpler and less expensive to implement than the resistance method. The resistance method requires electrical contacts with sufficiently low contact electrical resistance, thus necessitating the use of relatively expensive conductive agents (such as silver paint) and the removal of any paint or coating prior to the application of the electrical contacts to the cement-based material. Furthermore, reliable measurement of the electrical resistance requires four electrical contacts, with the outer two contacts for passing current and the inner two contacts for measuring the voltage. By using four contacts, the contact resistance essentially does not contribute to the measured resistance. If two contacts

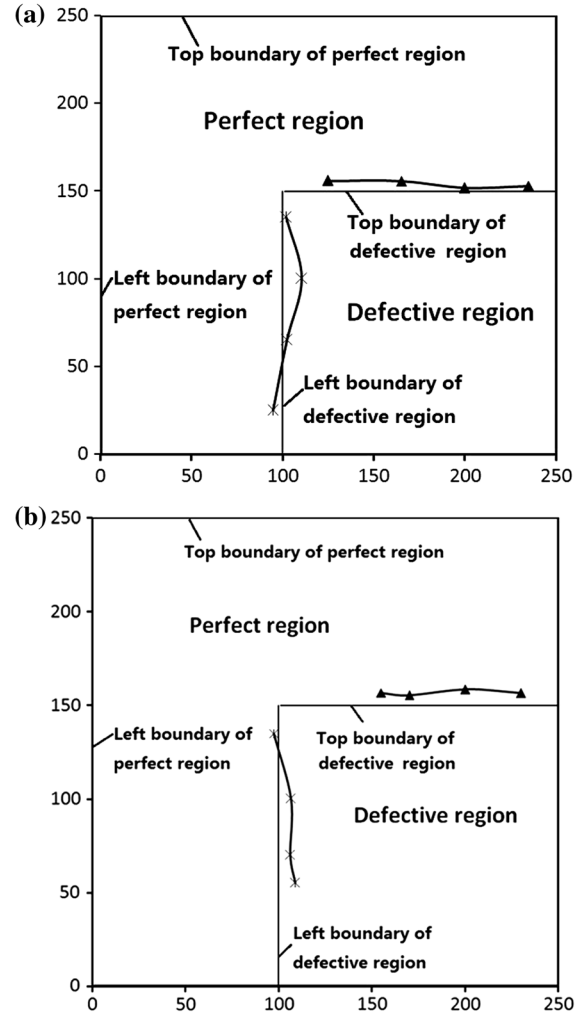

Fig. 9 Locus of the interface positions determined using various electrode series that are all directed perpendicular to the interface but positioned at various locations along the length of the interface. The four determined interface positions along the left boundary of the defective region are shown by X; those along the top boundary of the defective region are shown by ▲. All dimensions are in mm. **a** Configuration A. **b** Configuration B

are used instead, the contact resistance is included in the measured resistance, thus causing the measured resistance to be not sufficiently reflective of the condition of the cement-based material being inspected. In contrast, capacitance measurement involves only two electrodes (electrical contacts). The two-electrode configuration is much simpler to implement than the four-electrode configuration.

4 Conclusion

This paper provides the first report of capacitance-based nondestructive defect detection for a cement-based material. It is based on the use of the fringing electric field (2 kHz) of a capacitor that comprises the cement-based material (cement paste slab, $250 \times 250 \times 9.31$ mm^3) and two copper electrodes that are separated from the slab by an electrically insulating film held by adhesion and that is much smaller in area than the slab. The film is used because an RLC meter is not designed for measuring the capacitance of a conductive material. (The necessity of the film depends on the conductivity of the particular cement-based material.) Due to the strong fringing field emanating from the electrodes and going through the cement-based slab, the apparent permittivity is high, thus enabling the measured capacitance to be sensitive to defects in the slab.

The through-thickness capacitance, which relates to the apparent relative permittivity of the cement-based material, is measured using electrodes that sandwich the slab (configuration A). In contrast, the in-plane capacitance is measured using closely spaced parallel electrodes on the same surface of the slab (configuration B). The defective region ($150 \times 150 \times 9.31$ mm^3) of the slab is rendered defective by containing gypsum pellets (density 0.8385 g/cm^3 and average size 4.3 mm), the porosity of which causes the apparent relative permittivity of the defective region (142) to be lower than that of the adjacent perfect region (199).

To determine the position of the boundary of the defective region, the capacitance is measured using a series of electrodes, with each electrode geometry consisting of N squares (25×25 mm^2) linearly aligned perpendicular to the boundary. The capacitance is measured in order of increasing N, which is sufficient for the electrode to cover the regions on the two sides of the boundary. The capacitance increases linearly with N in each region, with the slope being different for the two regions, due to the difference in apparent permittivity. The slope (which excludes the influence of the capacitance associated with the electrodes) rather than the capacitance value (which includes the influence of the electrodes) is used as the indicator. The intersection of the extrapolated linear curves of the two regions gives the position of the boundary. The in-plane capacitance increases with decreasing spacing between the electrodes. With spacing 15 mm, the capacitance per unit electrode area is 0.157 and 0.105 pF/mm^2 for the perfect and defective regions, respectively.

Compliance with ethical standards

Conflict of interest Author Wang has received funding from the Education Department of Fujian Province and Wuyi University in partial support of this work.. The authors declare that they have no conflict of interest.

References

1. Heifetz A, Bakhtiari S, Lu J, Aranson IS, Vinokur VM, Bentivegna AF (2017) Development of microwave and impedance spectroscopy methods for in-situ nondestructive evaluation of alkali silica reaction in concrete. In: AIP conference proceedings 2017, vol 1806 (1, 43rd annual review of progress in quantitative nondestructive evaluation, 2016), pp 120003/1–120003/9
2. Al-Mattarneh H (2016) Determination of chloride content in concrete using near- and far-field microwave non-destructive methods. Corrosion Sci 105:133–140
3. Yildirim G, Aras Gulsum H, Banyhussan QS, Sahmaran M, Lachemi M (2015) Estimating the self-healing capability of cementitious composites through non-destructive electrical-based monitoring. NDT&E Int 76:26–37
4. Kusak I, Lunak M (2014) Comparison of impedance spectra of concrete recorded with utilizing carbon transition paste. Adv Mater Res 897:131–134
5. Garboczi EJ, Stutzman PE, Wang S, Martys NS, Hassan AM, Duthinh D, Provenzano V, Chou SG, Plusquellic DF, Surek JT, Kim S, McMichael RD, Stiles MD (2014) Corrosion detection in steel-reinforced concrete using a spectroscopic technique. In: AIP conference proceedings of 2014, vol 1581 (1, 40th annual review of progress in quantitative nondestructive evaluation; 10th conference on barkhausen noise and micromagnetic testing, 2013), pp 769–772
6. du Plooy R, Villain G, Palma LS, Ihamouten A, Derobert X, Thauvin B (2015) Electromagnetic non-destructive evaluation techniques for the monitoring of water and chloride ingress into concrete: a comparative study. Mater Struct 48(1–2):369–386
7. Liu Z, Zhang Y, Jiang Q, Zhang W, Wu J (2014) Solid phases percolation and capillary pores depercolation in hydrating cement pastes. J Mater Civil Eng 26(12):04014090/1–04014090/10
8. Andrade C, Briz S, Sanchez J, Zuloaga P, Navarro M, Ordonez M (2014) Evolution of corrosion parameters in a buried pilot nuclear waste container in el Cabril. MRS Online Proc Libr 1665:1–10
9. Hao B, Dou Y, Zeng D, Zeng Q (2014) Linear polarization method research of quantitative detection based on concrete reinforcement corrosion. Applied Mech Mater 526:64–69

10. Kessler S, Fischer J, Straub D, Gehlen C (2014) Updating of service-life prediction of reinforced concrete structures with potential mapping. Cem Concr Compos 7:47–52
11. Karaiskos G, Tsangouri E, Aggelis DG, Van Tittelboom K, De Belie N, Van Hemelrijck D (2016) Performance monitoring of large-scale autonomously healed concrete beams under four-point bending through multiple non-destructive testing methods. Smart Mater Struct 25(5):055003/1–055003/16
12. Chen J, Bharata R, Yin T, Wang Q, Wang H, Zhang T (2017) Assessment of sulfate attack and freeze-thaw cycle damage of cement-based materials by a nonlinear acoustic technique. Mater Struct 50(2):1–10
13. Ju T, Achenbach JD, Jacobs LJ, Guimaraes M, Qu J (2017) Ultrasonic nondestructive evaluation of alkali-silica reaction damage in concrete prism samples. Mater Struct 50(1):1–13
14. Carette J, Staquet S (2016) Monitoring and modelling the early age and hardening behaviour of eco-concrete through continuous non-destructive measurements: part II. Mechanical behavior. Cem Concr Compos 73:1–9
15. Smokotin A, Bogatyreva M, Protasova I (2016) The quality evaluation of concrete structures with the ultrasonic low-frequency tomograph. J Phys 671:012008/1–012008/6
16. Karaiskos G, Deraemaeker A, Aggelis DG, Van Hemelrijck D (2015) Monitoring of concrete structures using the ultrasonic pulse velocity method. Smart Mater Struct 24(11):113001/1–113001/18
17. Chen J, Ren J, Yin T (2016) Nondestructive evaluation of notched cracks in mortars by nonlinear ultrasonic technique. Nondestruct Test Eval 31(2):109–121
18. Ishibashi A, Matsuyama K, Alver N, Suzuki T, Ohtsu M (2016) Round-robin tests on damage evaluation of concrete based on the concept of acoustic emission rates. Mater Struct 49(7):2627–2635
19. Genoves V, Gosalbez J, Miralles R, Bonilla M, Paya J (2015) Ultrasonic characterization of GRC with high percentage of fly ash substitution. Ultrasonics 60:88–95
20. Kim G, In C, Kim J, Jacobs LJ, Kurtis KE (2014) Nondestructive detection and characterization of carbonation in concrete. AIP Conference Proceedings, vol 1581 (1, 40th annual review of progress in quantitative nondestructive evaluation; 10th conference on barkhausen noise and micromagnetic testing, 2013), pp 805–813
21. Hsieh C, Lin Y, Lin S (2017) Impact-echo method for the deterioration evaluation of near-surface mounted CFRP strengthening under outdoor exposure conditions. Mater Struct 50(1):1–10
22. Lider VV (2015) X-ray holography. Phys Usp 58(4):365–383
23. Palosaari MRJ, Kaeyhkoe M, Kinnunen KM, Laitinen M, Julin J, Malm J, Sajavaara T, Doriese WB, Fowler J, Reintsema C, Swetz D, Schmidt D, Ullom JN, Maasilta IJ (2016) Broadband ultrahigh-resolution spectroscopy of particle-induced X rays: extending the limits of nondestructive analysis. Phys Rev Appl 6(2):024002/1–024002/10
24. Jin Z, Zhao X, Zhao T, Yang L (2016) Corrosion and 3D crack-propagation behaviors in reinforced concrete subjected to bending load in simulated marine environment. Int J Electrochem Sci 11(10):8779–8796
25. Dasgupta P, Mondal BN (2016) Non-destructive quantitative analysis of five commercially available Indian cement clinkers using powder XRD. J Indian Chem Soc 93(2):193–197
26. Yang L, Zhang Y, Liu Z, Zhao P, Liu C (2015) In-situ tracking of water transport in cement paste using X-ray computed tomography combined with CsCl enhancing. Mater Lett 160:381–383
27. Landis EN, Bolander JE (2012) Microstructure and nondestructive evaluation: what we can measure, and what does it mean for the concrete life cycle. In: RILEM Proceedings of 2012; PRO 83 (2nd international conference on microstructural-related durability of cementitious composites, 2012), pp 951–959
28. Han J, Sun W, Pan G (2012) Analysis of different contents of blast-furnace slag effect on carbonation properties of hardened binder paste using micro-XCT technique. In: RILEM proceedings of 2012; PRO 83(2nd international conference on microstructural-related durability of cementitious composites, 2012), pp 1–7
29. Priyada P, Ramar R (2013) Application of gamma ray scattering technique for non-destructive evaluation of voids in concrete. Appl Radiat Isot 74:13–22
30. Tang P, Alqassim M, Daeid NN, Berlouis L, Seelenbinder J (2016) Nondestructive handheld fourier transform infrared (FT-IR) analysis of spectroscopic changes and multivariate modeling of thermally degraded plain portland cement concrete and its slag and fly ash-based analogs. Appl Spectrosc 70(5):923–931
31. Elbahi B, Boukli Hacene SMA (2016) Influence of limestone fillers and natural pozzolan on engineering properties of concrete. J Adhesion Sci Technol 30(16):1795–1807
32. Morsy R, Marzouk H, Gu X, Elshafey A (2016) Use of the random decrement technique for nondestructive detection of damage to beams. Mater Struct 49(11):4719–4727
33. Mohamad G, do Carmo PIO, de Oliveira MJD, Temp AL (2015) A combination method for evaluation of the concrete strength. Revista Materia 20(1):83–99
34. Breccolotti M, Bonfigli MFI (2015) An improved NDT method to evaluate the in situ strength of carbonated concrete. Nondestruct Test Eval 30(4):327–346
35. Garbacz A (2015) Application of stress based NDT methods for concrete repair bond quality control. Bull Polish Acad Sci Tech Sci 63(1):77–85
36. Montoya BM, DeJong JT (2015) Stress-strain behavior of sands cemented by microbially induced calcite precipitation. J Geotech Geoenviron Eng 141(6):1–10
37. Tong J, Chiu C, Wang C, Liao S, Wang H (2015) Using the synthetic aperture focusing technique with velocity responses to detect the defects inside reinforced concrete structures. J Chinese Inst Eng 38(5):636–644
38. Brozovsky J (2014) High-strength concrete—NDT with rebound hammer: influence of aggregate on test results. Nondestruct Test Eval 29(3):255–268
39. Zhao H, Huang D, Wang X, Chen X (2014) Dynamic elastic modulus of cement paste at early age based on nondestructive test and multiscale prediction model. J Wuhan Univ Technol Mater Sci Ed 29(2):321–328
40. Haddad RH, Odeh RA, Amawi HA, Ababneh AN (2013) Thermal performance of self-compacting concrete:

destructive and nondestructive evaluation. Can J Civil Eng 40(12):1205–1214
41. Ujike I, Okazaki S (2012) Study on obtaining quantitative index to evaluate durability of cover concrete. In: RILEM Proceedings of 2012; PRO 83(2nd international conference on microstructural-related durability of cementitious composites, 2012), pp 1558–1566
42. Kogbara RB, Iyengar SR, Grasley ZC, Masad EA, Zollinger DG (2015) Non-destructive evaluation of concrete mixtures for direct LNG containment. Mater Design 82:260–272
43. Borgharts JJAM, Pel L (2012) Non-destructive measurement of chloride in concrete by NMR. In: RILEM Proceedings of 2012; PRO 83(2nd international conference on microstructural-related durability of cementitious composites, 2012), pp 1–8
44. Cao J, Chung DDL (2002) Damage evolution during freeze-thaw cycling of cement mortar, studied by electrical resistivity measurement. Cem Concr Res 32(10):1657–1661
45. Cao J, Wen S, Chung DDL (2001) Defect dynamics and damage of cement-based materials, studied by electrical resistance measurement. J Mater Sci 36(18):4351–4360
46. Wen S, Chung DDL (2001) Electric polarization in carbon fiber reinforced cement. Cem Concr Res 31(2):141–147
47. Cao J, Chung DDL (2004) Electric polarization and depolarization in cement-based materials, studied by apparent electrical resistance measurement. Cem Concr Res 34(3):481–485
48. Wen S, Chung DDL (2001) Effect of stress on the electric polarization in cement. Cem Concr Res 31(2):291–295
49. Wen S, Chung DDL (2002) Cement-based materials for stress sensing by dielectric measurement. Cem Concr Res 32(9):1429–1433
50. Wen S, Chung DDL (2001) Effect of admixtures on the dielectric constant of cement paste. Cem Concr Res 31(4):673–677
51. Wang Y, Chung DDL (2017) Effect of the fringing electric field on the apparent electric permittivity of cement-based materials. Compos B 126:192–201
52. Cao J, Chung DDL (2004) Microstructural effect of the shrinkage of cement-based materials during hydration, as indicated by electrical resistivity measurement. Cem Concr Res 34(10):1893–1897
53. Xu Y, Chung DDL (2000) Improving silica fume cement by using silane. Cem Concr Res 30(8):1305–1311
54. Xu Y, Chung DDL (2000) Cement-based materials improved by surface treated admixtures. ACI Mater J 97(3):333–342
55. http://www.engineeringtoolbox.com/relative-permittivity-d_1660.html (as viewed on May 15, 2017)